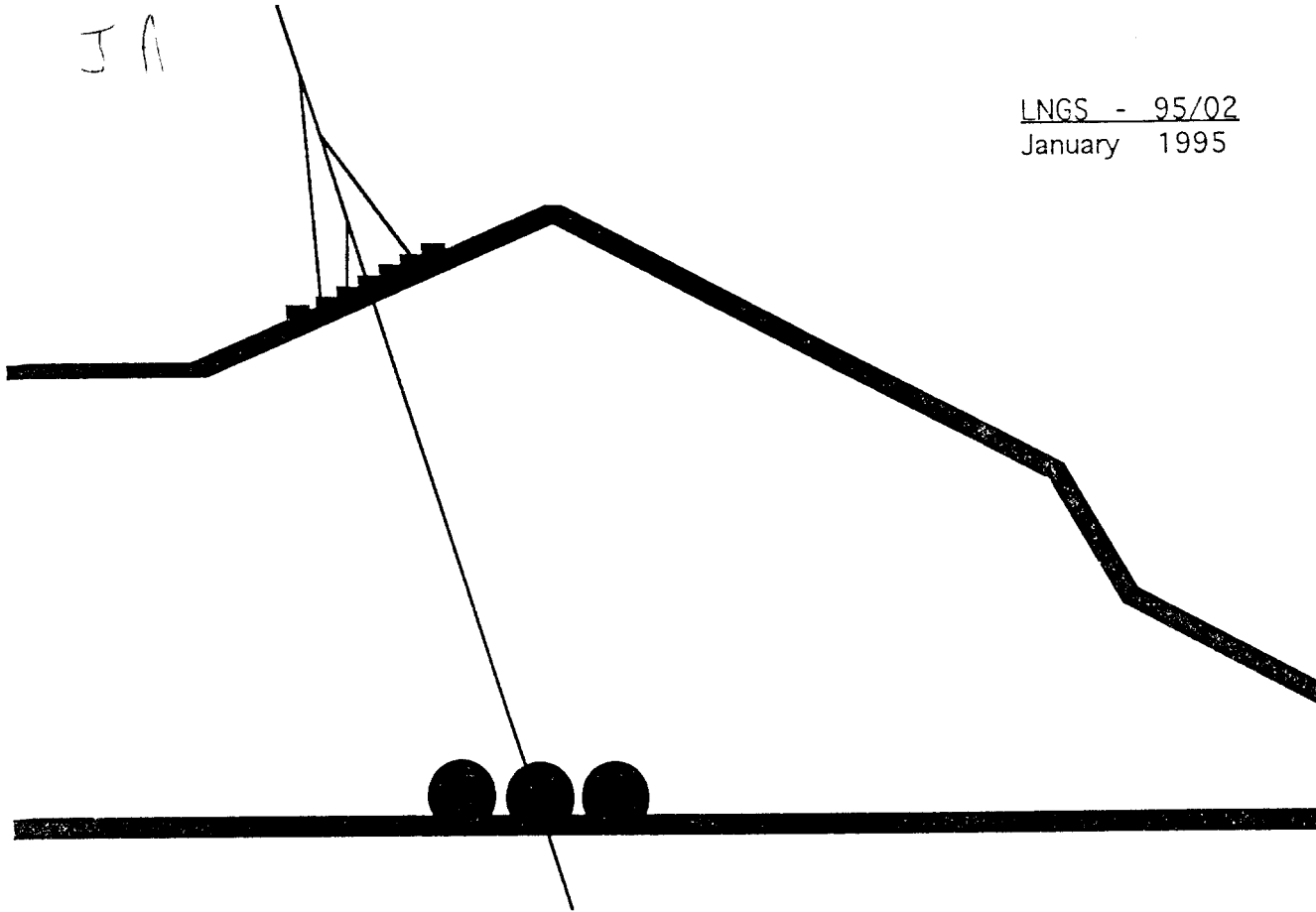


JA

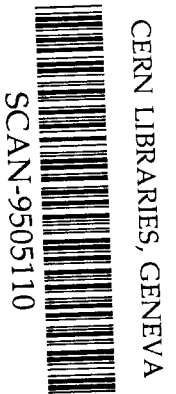
LNGS - 95/02
January 1995



A Measurement of the Negative Muon Spectrum between 0.3 and 40 GeV/c in the Atmosphere

R. Bellotti et al.

Submitted to Journal of Geophysical Researches



sw 95 87

INFN - Laboratori Nazionali del Gran Sasso

A Measurement of the Negative Muon Spectrum between 0.3 and 40 GeV/c in the Atmosphere

R. Bellotti,¹ F. Cafagna,¹ M. Circella,¹ G. De Cataldo,¹ C. N. De Marzo,¹ N. Giglietto,¹ P. Spinelli,¹ R. L. Golden,² S. A. Stephens,^{2,3} S. J. Stochaj,² W. R. Webber,² M. P. De Pascale,⁴ A. Morselli,⁴ P. Picozza,⁴ J. F. Ormes,⁵ R. E. Streitmatter,⁵ F. Massimo Brancaccio,⁶ P. Papini,⁶ P. Piccardi,⁵ P. Spillantini,⁶ G. Basini,⁷ F. Bongiorno,^{7,8} M. Ricci,⁷ M. T. Brunetti,⁹ A. Codino,⁹ C. Grimani,⁹ M. Menichelli,⁹ and I. Salvatori⁹

Received _____: accepted _____

Short title: NEGATIVE MUON SPECTRA IN THE ATMOSPHERE

¹Dipartimento di Fisica dell'Università di Bari and INFN-Sezione di Bari, Bari, Italy.

²Particle Astrophysics Laboratory, New Mexico State University, Las Cruces, New Mexico.

³Tata Institute of Fundamental Research, Bombay, India.

⁴Dipartimento di Fisica dell'Università di Roma "Tor Vergata" and INFN-Sezione di Roma II, Rome, Italy.

⁵NASA Goddard Space Flight Center, Greenbelt, Maryland.

⁶Dipartimento di Fisica dell'Università di Firenze and INFN-Sezione di Firenze, Florence, Italy.

⁷INFN Laboratori Nazionali di Frascati, Frascati, Italy.

⁸Dipartimento di Elettronica della III Università di Roma, Rome, Italy.

⁹Dipartimento di Fisica dell'Università di Perugia and INFN-Sezione di Perugia, Perugia, Italy.

Abstract. A measurement of the negative muon flux in the atmosphere has been made using a superconducting magnet spectrometer during the ascent part of a balloon flight experiment performed on September 5, 1989 from Prince Albert, Saskatchewan (Canada). The negative muon component has been measured over the momentum range 0.3–40 GeV/c with altitude increasing from 0.6 to 36 km above sea-level. This is the first time that results from such wide intervals in momentum and atmospheric depth have been obtained using a single apparatus. The flux growth curve with atmospheric depth is momentum dependent; the low energy muon flux peaks around 150 g/cm² and higher energy muons penetrate to larger depths in the atmosphere. The flux decreases exponentially with increasing depth above 200 g/cm². The attenuation length Λ_e increases almost linearly with the muon momentum at a rate of about 90 (g/cm²)/(GeV/c) in the 0.3–8 GeV/c range. The momentum spectra at different altitudes can be described by power-laws, provided that the spectral index is left free to change with altitude. We found that an index value of -2.5 ± 0.2 can give a good description of the data for momenta between 2 and 40 GeV/c in the depth range 20–400 g/cm². Below 1 GeV/c, the spectrum gradually steepens as the atmospheric depth decreases. Above 600 g/cm² a peak around 0.5 GeV/c arises.

1. Introduction

The main source of muons in the atmosphere in the momentum range below 40 GeV/c is the decay of pions produced in hadronic interactions of cosmic rays [e.g., *Badhwar et al.*, 1977]. The contribution from kaon decay is only important above a few hundred GeV/c. Recently, the opportunity to use this information as a check on cosmic ray cascade calculations and for calibration of the atmospheric neutrino calculations has created a renewed interest in the muon spectra as a function of the atmospheric depth [e.g., *Gaisser*, 1993; *Lipari*, 1993]. Preliminary values of the measurements presented in this paper have been already used as input data to calculations of the atmospheric neutrino flux with the hope to shed light on the problem of atmospheric neutrino anomaly [*Perkins*, 1994].

Detailed calculations of the muon flux in the atmosphere are very difficult to perform, especially at low energy where one needs to take into account the details of particle propagation and interactions. Analytic approaches have been successfully undertaken in the past since the pioneering work by *Stephens* [1981] [see also *Lipari*, 1993], even though Monte Carlo techniques are usually preferred.

While sea-level measurements are widely reported in the literature, there are very few measurements of the muon flux as a function of altitude [*Conversi*, 1950; *Blokh et al.*, 1977]. The latter experiments were carried out either with airplane-borne apparatus or at mountain sites. Counter telescopes were used for detecting charged particles and muons were selected by requiring them to traverse large amounts of matter without interacting. The main difficulty in performing a muon measurement at or above stratospheric altitudes is to properly compensate for the contamination of the muon sample by other particles. This problem becomes even more complex for positive muon measurements, since the proton flux strongly increases with altitude.

This paper reports a study of the atmospheric muon flux at various altitudes from 0.6 to 36 km carried out by analyzing the events recorded by the Matter Antimatter

Spectrometer System (MASS) apparatus during its ascent in a balloon flight. Although the main objective of the mission was to measure the antiproton flux at the top of the atmosphere, the apparatus was able to recognize negative muons with good efficiency and low background, as shown in the next sections. The sample of 2893 negative muons obtained at various altitudes provides the most extensive observation in the literature. The experiment was performed on September 5, 1989 starting from Prince Albert, Saskatchewan (Canada) at 600 m above sea-level. The coordinates of this location are 53°N and 106°W , corresponding to a cut-off rigidity of about 0.65 GV. The apparatus reached a float altitude of about 36 km after an ascent that lasted almost three hours. The data sample included more than 360,000 events, gathered over a period of 9855 s. Results on the negative muon spectrum in the momentum interval 0.3–40 GeV/c are presented in this paper. Preliminary results of this analysis were reported earlier [*Circella et al.*, 1993]. A measurement of the muon flux and charge ratio at the ground level has already been published [*De Pascale et al.*, 1993].

2. The MASS Apparatus

The MASS apparatus, shown in Figure 1, consisted of (1) a superconducting magnetic rigidity spectrometer using 8 multiwire proportional chambers (MWPC), (2) a time of flight (TOF) system with 2 planes having 2 layers each of scintillators to indicate the direction of travel, (3) a high resolution scintillator for ionization loss rate measurement, and (4) a gas Cherenkov detector and (5) a streamer tube imaging calorimeter to aid in particle identification. A coincidence between the TOF scintillators gave the trigger for data acquisition.

The superconducting magnet was operated at a current of 120 A, producing a magnetic field of 10 to 40 kG in the MWPC region. The maximum detectable rigidity for this configuration of the spectrometer was more than 100 GV [*Golden et al.*, 1991]. The MWPC signals were fed to delay lines and the times of arrival at each end of the

delay lines were measured [*Lacy and Lindsey, 1974*]. The sum of the delay line readout times was required to be equal to the total delay of the line, in order to accept an event. All of the chambers were equipped with a readout along the x-axis (where most of the curvature occurred) and four of them were also read in the y-view.

The Cherenkov detector was filled with a 50-50 mixture of Freon 12 and Freon 22 with a threshold Lorentz factor $\gamma_{th} \approx 23$. Signals from the TOF scintillators, the high resolution scintillator and the Cherenkov detector were pulse height analyzed.

The calorimeter consisted of 40 layers of 64 brass streamer tubes each. Tubes from adjacent layers were arranged perpendicular to each other. The total depth of the calorimeter was 40 cm, equivalent to 7.3 radiation lengths and 0.7 interaction lengths for protons. More details on the apparatus characteristics and performances are given elsewhere [*Golden et al., 1990; Golden et al., 1991; De Pascale et al., 1993*].

3. Data Analysis

3.1 Event Selection

All of the criteria used for event selection are reported in Table 1. Both reliability tests on the track reconstruction and muon identification criteria were considered. For the former purpose, tests 1 through 3 in Table 1 were found to be essential [see *Golden et al., 1991*, for an extensive discussion]. Tests 4 and 5 were introduced for selection of the muon signal against background with cuts on the pulse height distribution in the scintillators and the hit tube pattern in the calorimeter: muons were required to appear as minimum ionizing singly charged particles in two layers of scintillators (hereinafter referred to as T1 and T3, respectively) and not to show an interaction in the calorimeter. The latter condition was imposed by considering the calorimeter divided into two nearly equal upper and lower parts and by selecting events with a proper number of hits in each part—the lower y-view part was not operated during the flight. The symbol I_0 in

test 4 stands for the mean pulse height in the scintillator for a minimum ionizing singly charged particle.

The velocity measurement from the time of flight as well as the Cherenkov pulse height were also considered in the analysis, as explained in the next subsection.

A total number of 3235 negative curvature events were found to pass the tests in Table 1 and were selected for further analysis.

3.2 Background Estimates and Corrections

A special care was devoted in estimating the degree of possible contamination of the measurements by particles other than muons. Possible background sources are listed in Table 2, along with the procedures adopted to correct for them. The estimated residual contamination that can affect the final results of the analysis is also shown. One may note that the contamination is expected to have a dependence on both altitude and energy. This dependence was carefully studied in order to make the necessary corrections.

Albedo events are upward-going positive particles faking a negative curvature in the magnetic field. Most of these events arise from low energy protons impinging at large zenith angles which are scattered upward in interactions below the apparatus. The 432 upward-going particles found in the whole sample of negative curvature events were mostly concentrated toward the low atmospheric depths and around rigidities of 0.4 GV. The criteria used for muon selection and the scintillator test in particular were found to be very effective in order to remove these events. The few upward-going particles that survived the prior selection were finally rejected by means of a direct test of the β measurement from the time of flight, as shown in Table 2.

The electron flux in the atmosphere consists of a primary and a secondary component, the relative contributions to the total flux depending on the altitude and the energy of the particles. For energies ≤ 1 GeV, a broad peak is reached at atmospheric

depths of 100–150 g/cm² and the flux will rapidly decrease with increasing depth after this maximum [Allkofer and Grieder, 1984, and references therein]. The muon flux is expected to reach its maximum value deeper in the atmosphere. Also, the momentum spectrum is expected to be less steep for muons than for electrons at low momentum [Daniel and Stephens, 1974; Badhwar *et al.*, 1977]. For these reasons, it may be expected that the worst conditions for the relative ratio of muon to electron flux will occur at the lowest momentum and at less than 100 g/cm².

The degree of possible contamination of the muon sample by electrons can be realized from Figure 2, in which the fraction of muon-like events which are accompanied with a Cherenkov signal is shown. The events in Figure 2 were selected with the muon selection criteria (tests 1 through 5 in Table 1) and were also required to pass the β requirement in Table 2. The threshold rigidity for muons to give a Cherenkov signal occurs at 2.4 GV. Muon-like events with a Cherenkov signal far below this threshold were interpreted as contaminating electrons and removed from the sample. They are mostly distributed at very low rigidities and their number goes rapidly to zero above 1 GV. The fraction of events which were accompanied with a Cherenkov signal reached a value of 97% in the rigidity interval 4–8 GV, which increased to more than 98% if only the events passing through the central part of the detector were selected for this purpose. The latter result is quite consistent with the value of detector efficiency which was determined previously [Golden *et al.*, 1990]. From an assumed inefficiency of 3% for detecting particles far above the threshold and the ratio in Figure 2, the residual low energy electron contamination in Table 2 can be estimated.

The fraction of events with a Cherenkov signal from Figure 2 shows a value of 90% at rigidities greater than 8 GV. Spill-over may be responsible for this smaller value. If a Cherenkov efficiency of 97% is assumed, a total of 13 contaminating events can be estimated in the 8–100 GV interval, which is not inconsistent with the 16 spill-over events expected in this region.

Spill-over events are particles whose sign is misinterpreted in the magnet spectrometer. This situation can occur more easily at high rigidity, where the track curvature becomes comparable to the measurement resolution of the MWPC's. The number of expected spill-over events was estimated by convolution of the spectrum of positive particles surviving the negative muon selection with the resolution function of the spectrometer. It was found that spill-over may become a major source of background at rigidities greater than 8 GV, especially at small atmospheric depths where the proton flux is larger. The number of expected spill-over events was subtracted from the high energy muon sample. No correction was necessary at lower momenta.

Finally, in the meson (namely, pion and kaon) case, the relative ratio of fluxes can also be expected to be a function of altitude and energy. After a comparison of the present results to theoretical calculations of meson fluxes at several altitudes and energies in the atmosphere [*Badhwar et al.*, 1977], it was estimated that an altitude dependent pion contamination of the order of 1–2% could be present in the muon sample in the depth interval 25–250 g/cm². The kaon contamination will be much smaller and therefore absolutely negligible for this analysis.

3.3 Geometric Factor and Efficiencies

The geometric factor of the apparatus was calculated for particles that entered from the uppermost layer of the TOF scintillators and left through the bottom layer of the calorimeter. It is a function of particle rigidity and it ranges from 77.6 cm² sr at 0.3 GV to 127.8 cm² sr at $R \geq 5$ GV for negative particles. There exists a small difference between positive and negative particles due to a mechanical asymmetry of the magnet with respect to the detector stack. The geometric factor calculations are accurate to the order of 0.1%. The MWPC efficiency also shows a dependence on deflection, as discussed in *De Pascale et al.* [1993]. It increases from 0.51 ± 0.03 at about 0.3 GV to a plateau value of 0.69 ± 0.01 above 2 GV for negative particles.

Signals from one layer of the upper set of scintillators and one of the lower set were considered for event selection. Such a combination can help improve the rejection of non-minimum ionizing particles because of the small amount of energy (≈ 10 MeV at minimum ionization) that a particle will lose while traversing the apparatus and it can have a larger effect on the selection of low energy positive muons. The scintillator efficiency was studied with the aid of the signal from the high resolution scintillator S1. The float altitude high energy proton sample was considered for this purpose and their pulse heights from S1, T1 and T3 carefully studied. Finally, an efficiency of 89% was estimated for the scintillator selection, which is quite consistent with previous studies [*De Pascale et al.*, 1993].

The calorimeter efficiency for detection of non interacting particles which satisfy Test 5 in Table 1 was studied by carefully examining the topology of each event which failed to pass the requirement. The streamer tube inefficiency as well as the noise can lead to a failure of the test. A global selection efficiency of 80% was estimated, in good agreement with what found in the ground analyses [*De Pascale et al.*, 1993]. Also, a large sample of particles passing Test 5 were scanned, in order to check for interacting particle contamination. No evidence of electromagnetic showers or interactions in the calorimeter was found in the muon sample at rigidities larger than 1.5 GV. The time dependence of both the calorimeter and scintillators responses was accurately studied and no significant variation with time was observed.

The velocity selection, as in Table 2, introduced a 98% efficiency, because some configurations of the scintillator paddles were not suitable for a TOF measurement and as a consequence a fraction of the events had to be removed from the analysis. Efficiencies were also introduced in order to compensate for the tape transferring process (97%) and trigger efficiency (82%) [*De Pascale et al.*, 1993]. On the contrary, no correction was necessary for the Cherenkov test at low energy since the probability for a particle below threshold to be accompanied with a noise pulse larger than the equivalent

to 1 photoelectron had been estimated to be negligible [*Golden et al.*, 1990].

In evaluating the absolute fluxes, the exposure time as well as the dead-time fraction was considered. The latter was time-dependent since the trigger rate changed considerably during the ascent. The recording efficiency due to the dead-time (hereinafter referred to as “live-time fraction”) varied between 0.98 at altitudes close to ground and 0.68 at float altitude. It changed slowly at altitudes greater than 15 km (atmospheric depths less than 130 g/cm²).

All of the efficiencies considered in this analysis are reported in Table 3, along with the estimated errors, if not negligible. The global efficiency for detection of negative muons ranged from 0.184 ± 0.011 at 300 MeV/c at maximum dead-time to 0.375 ± 0.009 above 2 GeV/c at minimum dead-time. For the global systematic uncertainty on the detection efficiency we can set an upper limit at 5%, based on our knowledge of the apparatus used in these as well as in other measurements. Both statistical fluctuations of the number of events and the estimated uncertainties of the detection efficiencies are included in the results. Gaussian errors were assumed for muon event fluctuations and also for background events.

4. Results

A sample of 2893 negative muons was finally selected with all of the criteria from Table 1 and Table 2, in the momentum range 0.3–40 GeV/c. Since they were recorded during the ascent of the flight, they were distributed between 910 and 5 g/cm² in atmospheric depth. Figure 3 shows the ascent curve of the apparatus, as measured during the NSBF (National Scientific Balloon Facility) control operation. The accuracy with which the atmospheric depth can be determined at each time is of the order of 1%.

4.1 Flux growth curve

The altitude dependence of the negative muon flux was separately investigated in different momentum intervals. Independent growth curves in the atmosphere were built in the different momentum bins, with the constraints imposed by the flux values at ground level and float altitude, as measured with the same apparatus [De Pascale *et al.*, 1993; Codino *et al.*, 1994]. It was found that a curve of the form:

$$\Phi(X) = kXe^{-X/\Lambda}, \quad (1)$$

Φ being the muon flux in a momentum bin, X being the atmospheric depth and k and Λ being free to change in order to best fit the data, can give a good interpolation of the measurements, except at very low momenta where the flux undergoes a sudden attenuation soon after reaching a maximum around 150 g/cm^2 .

The flux growth curves for nine momentum intervals are reported in Table 4. A growth curve as in (1) with the best-fit values of the parameters k and Λ was used for estimating the flux-weighted average values of atmospheric depth (FAD) shown along with the measured fluxes in Table 4. These results are plotted in Figure 4. Average values of atmospheric depth during the payload ascent (APD) are also shown in Table 4.

Investigations of the altitude dependence of the flux require small momentum intervals in order to have minimum spectral variations with changing altitudes. On the other hand, larger bin widths are preferred in order to minimize the statistical fluctuations, especially when dealing with small samples of events. The momentum intervals used in Table 4 are the best compromise between these two constraints. As a consequence, average values of momentum can be calculated in each momentum interval and the spectral variations with altitude will not affect these estimates more than the estimated statistical uncertainties (1–2 %, typically). They are shown in Figure 4.

As a close investigation of Figure 4 reveals, the flux growth curves do not scale

with the muon momentum. In particular, we note that the broad peak in the curves moves from around 150 g/cm^2 toward 200 g/cm^2 with increasing momentum from below $0.5 \text{ GeV}/c$ up to a few GeV/c . At the same time, the flatness of the growth curves at larger depths increases with increasing momenta. If a parametrization as in (1) is adopted, the best-fit value of Λ increases from $\Lambda = 192 \pm 3 \text{ g/cm}^2$ to $\Lambda = 216 \pm 3 \text{ g/cm}^2$ and $\Lambda = 268 \pm 4 \text{ g/cm}^2$, respectively in the intervals $0.3\text{--}0.75 \text{ GeV}/c$, $0.75\text{--}1.55 \text{ GeV}/c$ and $1.55\text{--}8 \text{ GeV}/c$. In this case, the average muon energy changes from below to above the energy ε_μ , at which the mean path of a muon before decaying equals the atmospheric scale height—being $\varepsilon_\mu \approx 1 \text{ GeV}$ at stratospheric depths [Gaisser, 1990]. The momentum dependence of the flux growth curve will correspond to an altitude dependence of the muon momentum spectra, as commented on in the next subsection.

Difficulties arise when trying to interpolate the measurements at low energy and high depth with a curve as in (1). Unfortunately, no detailed calculations are available in the literature in these ranges of energy and altitude for a cross-check of the theory as well as of the measurements. In a simplified model of the muon propagation in the atmosphere, taking into account the energy-losses and the energy-dependent muon decay probability, we calculated the muon spectrum on the ground from the lowest altitude measurements and vice-versa. We did not find any evidence of contradiction between the two sets of data.

It may be pointed out that an exponential attenuation can give a better interpolation of the measurements deep in the atmosphere than the growth curve in (1). Our best-fit values for the exponential attenuation length Λ_e in the $190\text{--}910 \text{ g/cm}^2$ range are $\Lambda_e = 345 \pm 17 \text{ g/cm}^2$, $\Lambda_e = 378 \pm 14 \text{ g/cm}^2$ and $\Lambda_e = 571 \pm 30 \text{ g/cm}^2$, in the intervals $0.3\text{--}0.75 \text{ GeV}/c$, $0.75\text{--}1.55 \text{ GeV}/c$ and $1.55\text{--}8 \text{ GeV}/c$, respectively. We also found an almost linear dependence of Λ_e with the average momentum of muons in the $0.3\text{--}8 \text{ GeV}/c$ range, with an increasing rate of about $90 \text{ (g/cm}^2)/(\text{GeV}/c)$.

Conversi [1950] investigated the altitude dependence of the muon and proton flux

in the depth range 231–1010 g/cm². Muons were identified by means of a delayed coincidence technique. They were stopped in a 10 cm graphite absorber, after traversing 6 inches of lead and the resulting momentum interval was 315–348 MeV/c. Corrections were introduced in order to refer all the measurements to the same latitude of 50°N. An exponential fit with an attenuation length $\Lambda_e = 280$ g/cm² was found to give a good interpolation of the total muon data. This value is not inconsistent with $\Lambda_e = 347 \pm 41$ g/cm² that we found for the ascent negative muon flux between 300 and 530 MeV/c in the depth range 190–910 g/cm². It should be noted that the flux dependence on altitude may be different for muons of different charges, reflecting the different interaction properties of protons and neutrons. Also, our average momentum is higher than in *Conversi* [1950].

Blokh et al. [1977] reported measurements of the muon flux between 600 and 1000 mbar taken on Mount Elbrus. They used a 10 cm lead shield with a resulting momentum threshold lower than 300 MeV/c. Only integral flux measurements of muons of either charges above this momentum threshold are available in this case, and therefore a comparison with either the present results or those by *Conversi* [1950] is difficult.

4.2 Momentum Spectrum

The negative muon momentum spectra at four different average atmospheric depths are shown in Figure 5. The data for this figure correspond to the depth interval between 250 and 25 g/cm², where the momentum dependence of the flux growth curve is so smooth that the differences among the mean atmospheric depths in different momentum intervals are much less than 1%, as can be seen in Table 4. In some cases, the flux-weighted average values of depth also differ negligibly from the corresponding average working depths of the apparatus and this is an indication that a linear dependence of the flux on the atmospheric depth can give a good approximation within the pressure interval considered. An accuracy of 1% has to be assumed on the

values of average atmospheric depth shown in Figure 5. The flux is plotted at mean momentum values from a flux-averaged estimate. A power-law distribution was assumed for this purpose:

$$\Phi(P) \propto P^\alpha, \quad (2)$$

with the power index α left free to change with momentum and depth in order to best fit the data. We found that, while below 1 GeV/c α gradually decreases from a small positive value above 600 g/cm² to ≈ -1 at the lowest atmospheric depth, it stays almost constant above 2 GeV/c, $\alpha = -2.5 \pm 0.2$ giving a good description of the spectrum between 20 and 400 g/cm².

5. Conclusions

A study of the muon component in the atmosphere has been carried out by means of a single apparatus during the ascent of a balloon flight at high latitude. The depth range covered in this experiment is between 5 and 910 g/cm². The momentum interval investigated ranges from 0.3 to 40 GeV/c. The altitude dependence of the negative muon flux has been studied in nine momentum intervals. It has been shown that the flux growth curve in the atmosphere does not scale with the muon momentum. Also, the negative muon momentum spectra have been measured in four depth ranges. Spectral variations, as well as intensity variations, have been found with changing altitude. However, an altitude-independent power-law representation of the data is possible at momenta between 2 and 40 GeV/c in a wide range of atmospheric depth.

To judge the consistency of the present measurements with the rather scanty previous data is not a straightforward matter, even though no contradiction seems to appear.

The measured spectra can provide constraints to, and improve the precision of

calculations of the atmospheric neutrino fluxes. Further information will be derived by an analysis of the positive muon data from the same flight. A new dedicated flight aimed at an extensive exploration of the secondary particles in the atmosphere with better statistical precision is being planned.

Acknowledgments. We would like to thank the National Scientific Balloon Facility (Palestine, Texas) for providing us with their measurements of the ascent curve of the apparatus.

This work was supported by NASA Grant NAG-110, the Istituto Nazionale di Fisica Nucleare, Italy, and the Agenzia Spaziale Italiana, as part of the research activities of the WIZARD collaboration. A very special thank to our technical support staff from NMSU and INFN.

References

- Allkofer, O. C., and P. K. F. Grieder, *Physics Data: Cosmic Rays on Earth*, Fachinformationszentrum, Karlsruhe, Germany, 1984.
- Badhwar, G. D., S. A. Stephens, and R. L. Golden, Analytic representation of the proton-proton and proton-nucleus cross-sections and its application to the sea-level spectrum and charge ratio of muons, *Phys. Rev. D*, *15*, 820, 1977.
- Blokh, Ya. L., L. I. Dorman, and I. Ya. Libin, Studies of the angular distribution and of the altitude dependence of the cosmic-ray muon and general components using scintillation telescopes, *Nuovo Cimento Soc. Ital. Fis.*, *37B*, 198, 1977.
- Circella, M., F. Cafagna, G. Basini, R. Bellotti, F. Bongiorno, M. T. Brunetti, A. Codino, C. N. De Marzo, M. P. De Pascale, R. L. Golden, C. Grimani, B. L. Kimbell, F. Massimo Brancaccio, M. Menichelli, A. Morselli, J. F. Ormes, P. Papini, P. Picozza, M. Ricci, I. Salvatori, E. S. Seo, P. Spillantini, S. A. Stephens, S. J. Stochaj, R. E. Streitmatter, and W. R. Webber, Cosmic ray muon spectrum in the atmosphere, *Conf. Pap. Int. Cosmic Ray Conf. 23rd. 4*, 503, 1993.
- Codino, A., G. Basini, F. Bongiorno, F. Massimo Brancaccio, M. T. Brunetti, R. L. Golden, C. Grimani, B. L. Kimbell, M. Menichelli, M. Miozza, A. Morselli, J. F. Ormes, P. Papini, M. P. de Pascale, P. Picozza, M. Ricci, I. Salvatori, P. Spillantini, S. A. Stephens, S. J. Stochaj, R. E. Streitmatter, and W. R. Webber, Negative pion and muon flux determination at an atmospheric depth of 5 g/cm², to appear in *Proc. of Vulcano Workshop 1994*, 1994.
- Conversi, M., Experiments on cosmic-ray mesons and protons at several altitudes and latitudes, *Phys. Rev.*, *79*, 749, 1950.
- Daniel, R. R., and S. A. Stephens, Cosmic-ray-produced electrons and gamma rays in the atmosphere, *Rev. Geophys. and Sp. Phys.*, *12*, 233, 1974.
- De Pascale, M. P., A. Morselli, P. Picozza, R. L. Golden, C. Grimani, B. L. Kimbell, S. A. Stephens, S. J. Stochaj, W. R. Webber, G. Basini, F. Bongiorno, F. M. Brancaccio,

- M. Ricci, J. F. Ormes, E. S. Seo, R. E. Streitmatter, P. Papini, P. Spillantini, M. T. Brunetti, A. Codino, M. Menichelli, and I. Salvatori, Absolute spectrum and charge ratio of cosmic ray muons in the energy region from 0.2 to 100 GeV at 600 m above sea-level, *J. Geophys. Res.*, *98*, 3501, 1993.
- Gaisser, T. K., *Cosmic Rays and Particle Physics*, Cambridge University Press, Cambridge, Mass., 1990.
- Gaisser, T. K., Atmospheric neutrino event rates: the expectations, Univ. of Delaware preprint BA-93-38, 1993.
- Golden, R. L., C. Grimani, B. L. Kimbell, W. R. Webber, G. Basini, A. Morselli, M. Ricci, J. F. Ormes, E. S. Seo, S. J. Stochaj, R. E. Streitmatter, P. Spillantini, A. Codino, M. Menichelli, M. P. De Pascale, F. Bongiorno, and P. Picozza, Performance of a focused gas Cherenkov detector used for cosmic ray studies, *PAL technical note nr. 224*, 1990, available on request.
- Golden, R. L., C. Grimani, B. L. Kimbell, W. R. Webber, G. Basini, A. Morselli, M. Ricci, J. F. Ormes, E. S. Seo, S. J. Stochaj, R. E. Streitmatter, P. Spillantini, A. Codino, M. Menichelli, M. P. De Pascale, F. Bongiorno, and P. Picozza, Performance of a balloon-borne magnet spectrometer for cosmic ray studies, *Nucl. Instrum. Meth.*, *A306*, 366, 1991.
- Lacy, J. L., and R. S. Lindsey, High resolution readout of multiwire proportional counters using the cathode coupled delay-line technique, *Nucl. Instrum. Meth.*, *119*, 483, 1974.
- Lipari, P., Lepton spectra in the earth's atmosphere, *Astropart. Phys.*, *1*, 195, 1993.
- Perkins, D. H., A new calculation of atmospheric neutrino fluxes, *Astropart. Phys.*, *2*, 249, 1994.
- Stephens, A. S., Secondary components of cosmic radiation at small atmospheric depths, *Conf. Pap. Int. Cosmic Ray Conf. 17th*, *4*, 282, 1981.

This manuscript was prepared with the AGU L^AT_EX macros v3.1.

Figure 1. The MASS apparatus.

Figure 2. Fraction of negative muon-like events accompanied with a Cherenkov signal as a function of rigidity.

Figure 3. Ascent curve of the apparatus.

Figure 4. Flux growth curves for negative muons in the 0.3–40 GeV/c momentum range. Results are plotted for various momentum intervals. The corresponding average values of momentum are shown. Some of the distributions have been scaled as indicated. The measurements at the highest and lowest depths are from *De Pascale et al.* [1993] and *Codino et al.* [1994], respectively. Best-fit curves of the form (1) are superimposed.

Figure 5. Negative muon momentum spectra at various depths in the atmosphere. The depth ranges are shown, and the corresponding average values as well. Some of the distributions have been scaled as indicated. Measurements at the ground level (960 g/cm²) and at 5 g/cm² atmospheric depth are also shown [*De Pascale et al.*, 1993, and *Codino et al.*, 1994, respectively].

Table 1. Selection criteria

Test	Description
1	A minimum of 5 out of 8 x-view and 3 out of 4 y-view MWPC's, with proper location in the spectrometer, giving good time sum measurements
2	$\chi_x^2 \leq 5$ and $\chi_y^2 \leq 7.5$ for the reconstructed track
3	A deflection uncertainty $\sigma_\eta \leq 0.03 \text{ GV}^{-1}$
4	Signals S from T1 and T3 such that: $0.5I_0 \leq S \leq 2I_0$
5	A number of hits N in the calorimeter such that: $2 \leq N \leq 9$ in the x- and y-view upper part and $3 \leq N \leq 12$ in the x-view lower part

Table 2. Background sources

Source	Correction	Residual contamination
Albedo	$\beta \geq 0.8$	none
Electrons	Cherenkov pulse height less than the equivalent to 1 photoelectron at rigidities $R \leq 1.5$ GV	$\leq 1\%$ at less than 1 GeV/c negligible at higher momenta
Spill-over protons	spill-over subtraction at rigidities $R \geq 8$ GV	negligible
Mesons	no correction	$\leq 1\%$ almost everywhere for pions negligible for kaons

Table 3. Apparatus efficiency

Detector or Function	Efficiency
MWPC	Energy-dependent below 2 GeV/c 0.69±0.01 above 2 GeV/c
Scintillators	0.89±0.01
Calorimeter	0.80±0.01
TOF	0.98
Tape Reading	0.97
Trigger	0.82±0.01
Live-time	Time-dependent Between 0.65 and 0.68 at less than 130 g/cm ²

Table 4. Flux growth curve results for negative muons in the 0.3–40 GeV/c momentum range

Depth Interval		A	B	C	D
Duration (s)		635	630	520	470
Live-time fraction		0.98	0.91	0.84	0.77
Initial depth (g/cm ²)		910	587	381	243
Final depth (g/cm ²)		587	381	243	190
APD (g/cm ²)		736	477	313	215
I	Flux	$1.93 \pm 0.70 \cdot 10^{-3}$	$4.9 \pm 1.1 \cdot 10^{-3}$	$1.12 \pm 0.20 \cdot 10^{-2}$	$1.46 \pm 0.26 \cdot 10^{-2}$
	FAD (g/cm ²)	702.6	466.0	309.6	215.1
II	Flux	$2.12 \pm 0.62 \cdot 10^{-3}$	$5.6 \pm 1.1 \cdot 10^{-3}$	$1.05 \pm 0.17 \cdot 10^{-2}$	$1.24 \pm 0.20 \cdot 10^{-2}$
	FAD (g/cm ²)	706.5	467.8	310.3	215.2
III	Flux	$2.10 \pm 0.59 \cdot 10^{-3}$	$5.6 \pm 1.0 \cdot 10^{-3}$	$8.3 \pm 1.4 \cdot 10^{-3}$	$1.00 \pm 0.17 \cdot 10^{-2}$
	FAD (g/cm ²)	707.4	468.1	310.5	215.3
IV	Flux	$2.08 \pm 0.52 \cdot 10^{-3}$	$4.50 \pm 0.81 \cdot 10^{-3}$	$6.1 \pm 1.1 \cdot 10^{-3}$	$8.4 \pm 1.4 \cdot 10^{-3}$
	FAD (g/cm ²)	708.9	468.8	310.8	215.3
V	Flux	$1.56 \pm 0.40 \cdot 10^{-3}$	$3.93 \pm 0.67 \cdot 10^{-3}$	$4.74 \pm 0.85 \cdot 10^{-3}$	$6.2 \pm 1.1 \cdot 10^{-3}$
	FAD (g/cm ²)	710.0	469.3	311.0	215.3
VI	Flux	$1.33 \pm 0.31 \cdot 10^{-3}$	$2.39 \pm 0.44 \cdot 10^{-3}$	$3.79 \pm 0.64 \cdot 10^{-3}$	$4.29 \pm 0.74 \cdot 10^{-3}$
	FAD (g/cm ²)	711.8	470.0	311.4	215.4
VII	Flux	$9.4 \pm 1.6 \cdot 10^{-4}$	$1.52 \pm 0.22 \cdot 10^{-3}$	$1.81 \pm 0.27 \cdot 10^{-3}$	$1.98 \pm 0.31 \cdot 10^{-3}$
	FAD (g/cm ²)	714.6	471.2	311.9	215.5
VIII	Flux	$3.17 \pm 0.47 \cdot 10^{-4}$	$4.32 \pm 0.58 \cdot 10^{-4}$	$4.03 \pm 0.64 \cdot 10^{-4}$	$4.36 \pm 0.72 \cdot 10^{-4}$
	FAD (g/cm ²)	719.7	473.4	312.9	215.6
IX	Flux	$2.37 \pm 0.50 \cdot 10^{-5}$	$2.00 \pm 0.48 \cdot 10^{-5}$	$1.76 \pm 0.51 \cdot 10^{-5}$	$1.74 \pm 0.56 \cdot 10^{-5}$
	FAD (g/cm ²)	723.9	475.1	313.6	215.7

Table 4. (continued)

Depth Interval		E	F	G	H
Duration (s)		430	490	560	600
Live-time fraction		0.72	0.69	0.68	0.67
Initial depth (g/cm ²)		190	149	120	92
Final depth (g/cm ²)		149	120	92	66
APD (g/cm ²)		169	133	107	78
I	Flux	$1.84 \pm 0.31 \cdot 10^{-2}$	$1.55 \pm 0.28 \cdot 10^{-2}$	$1.51 \pm 0.26 \cdot 10^{-2}$	$1.37 \pm 0.23 \cdot 10^{-2}$
	FAD (g/cm ²)	168.8	133.4	107.1	79.0
II	Flux	$1.09 \pm 0.20 \cdot 10^{-2}$	$1.11 \pm 0.20 \cdot 10^{-2}$	$9.4 \pm 1.7 \cdot 10^{-3}$	$8.3 \pm 1.6 \cdot 10^{-3}$
	FAD (g/cm ²)	168.8	133.5	107.1	79.0
III	Flux	$1.00 \pm 0.18 \cdot 10^{-2}$	$1.05 \pm 0.18 \cdot 10^{-2}$	$8.7 \pm 1.6 \cdot 10^{-3}$	$7.1 \pm 1.4 \cdot 10^{-3}$
	FAD (g/cm ²)	168.8	133.5	107.1	79.0
IV	Flux	$8.0 \pm 1.5 \cdot 10^{-3}$	$7.4 \pm 1.4 \cdot 10^{-3}$	$6.2 \pm 1.2 \cdot 10^{-3}$	$5.8 \pm 1.1 \cdot 10^{-3}$
	FAD (g/cm ²)	168.9	133.5	107.1	79.0
V	Flux	$5.6 \pm 1.1 \cdot 10^{-3}$	$4.97 \pm 0.98 \cdot 10^{-3}$	$3.90 \pm 0.82 \cdot 10^{-3}$	$3.70 \pm 0.78 \cdot 10^{-3}$
	FAD (g/cm ²)	168.9	133.5	107.1	79.0
VI	Flux	$3.98 \pm 0.77 \cdot 10^{-3}$	$3.80 \pm 0.72 \cdot 10^{-3}$	$3.01 \pm 0.61 \cdot 10^{-3}$	$2.86 \pm 0.58 \cdot 10^{-3}$
	FAD (g/cm ²)	168.9	133.5	107.1	79.0
VII	Flux	$2.15 \pm 0.35 \cdot 10^{-3}$	$2.14 \pm 0.33 \cdot 10^{-3}$	$1.76 \pm 0.28 \cdot 10^{-3}$	$1.33 \pm 0.24 \cdot 10^{-3}$
	FAD (g/cm ²)	169.0	133.6	107.2	79.1
VIII	Flux	$4.55 \pm 0.80 \cdot 10^{-4}$	$3.81 \pm 0.70 \cdot 10^{-4}$	$3.38 \pm 0.62 \cdot 10^{-4}$	$3.42 \pm 0.61 \cdot 10^{-4}$
	FAD (g/cm ²)	169.0	133.6	107.2	79.1
IX	Flux	$1.80 \pm 0.63 \cdot 10^{-5}$	$2.63 \pm 0.72 \cdot 10^{-5}$	$1.45 \pm 0.52 \cdot 10^{-5}$	$1.85 \pm 0.57 \cdot 10^{-5}$
	FAD (g/cm ²)	169.1	133.6	107.2	79.1

Table 4. (continued)

Depth Interval		I	J	K
Duration (s)		1180	1760	2580
Live-time fraction		0.66	0.67	0.68
Initial depth (g/cm ²)		66	36	15
Final depth (g/cm ²)		36	15	5
APD (g/cm ²)		49	24	9
I	Flux	$1.00 \pm 0.14 \cdot 10^{-2}$	$5.8 \pm 1.2 \cdot 10^{-3}$	$2.04 \pm 0.59 \cdot 10^{-3}$
	FAD (g/cm ²)	50.3	24.9	9.7
II	Flux	$6.34 \pm 0.99 \cdot 10^{-3}$	$4.07 \pm 0.70 \cdot 10^{-3}$	$1.26 \pm 0.37 \cdot 10^{-3}$
	FAD (g/cm ²)	50.4	24.9	9.7
III	Flux	$4.26 \pm 0.76 \cdot 10^{-3}$	$2.84 \pm 0.52 \cdot 10^{-3}$	$9.8 \pm 2.6 \cdot 10^{-4}$
	FAD (g/cm ²)	50.4	24.9	9.8
IV	Flux	$3.63 \pm 0.62 \cdot 10^{-3}$	$1.72 \pm 0.35 \cdot 10^{-3}$	$7.4 \pm 1.9 \cdot 10^{-4}$
	FAD (g/cm ²)	50.4	24.9	9.8
V	Flux	$2.98 \pm 0.50 \cdot 10^{-3}$	$1.48 \pm 0.29 \cdot 10^{-3}$	$6.3 \pm 1.5 \cdot 10^{-4}$
	FAD (g/cm ²)	50.4	24.9	9.8
VI	Flux	$2.23 \pm 0.37 \cdot 10^{-3}$	$1.02 \pm 0.20 \cdot 10^{-3}$	$3.41 \pm 0.95 \cdot 10^{-4}$
	FAD (g/cm ²)	50.4	24.9	9.8
VII	Flux	$8.6 \pm 1.4 \cdot 10^{-4}$	$3.22 \pm 0.69 \cdot 10^{-4}$	$1.87 \pm 0.43 \cdot 10^{-4}$
	FAD (g/cm ²)	50.4	24.9	9.9
VIII	Flux	$1.65 \pm 0.30 \cdot 10^{-4}$	$7.3 \pm 1.6 \cdot 10^{-5}$	$4.9 \pm 1.1 \cdot 10^{-5}$
	FAD (g/cm ²)	50.5	24.9	9.9
IX	Flux	$1.17 \pm 0.33 \cdot 10^{-5}$	$5.1 \pm 1.9 \cdot 10^{-6}$	$3.7 \pm 1.4 \cdot 10^{-6}$
	FAD (g/cm ²)	50.5	24.9	9.9

Results are given for the following momentum intervals (average values are shown in Figure 4): I 0.3–0.53 GeV/c, II 0.53–0.75 GeV/c, III 0.75–0.97 GeV/c, IV 0.97–1.23 GeV/c, V 1.23–1.55 GeV/c, VI 1.55–2 GeV/c, VII 2–3.2 GeV/c, VIII 3.2–8 GeV/c, IX 8–40 GeV/c. The symbols APD and FAD stand respectively for Average Payload Depth and Flux-weighted Average Depth in the momentum bin. The units of flux are particles/(cm² s sr GeV/c).

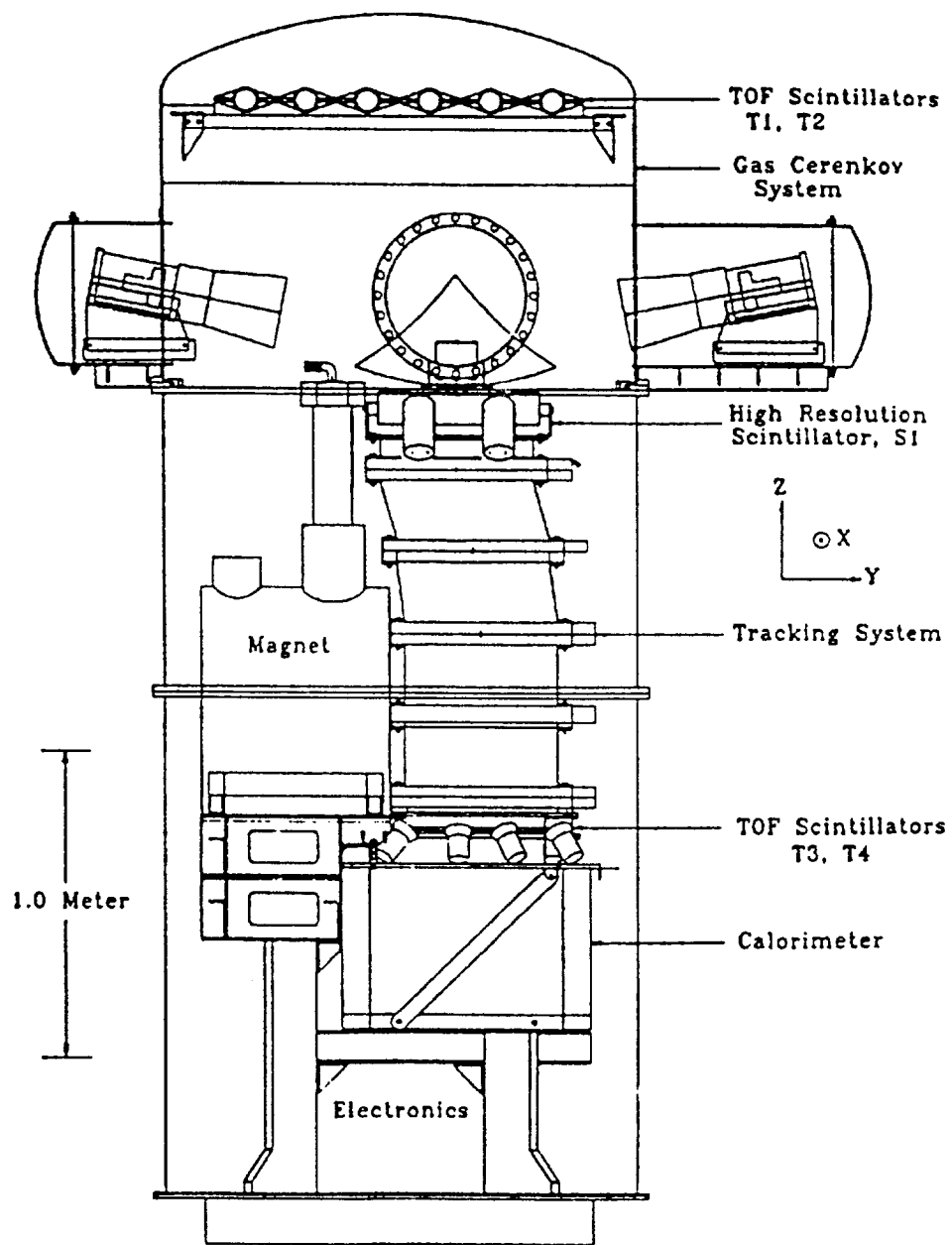


Figure 1

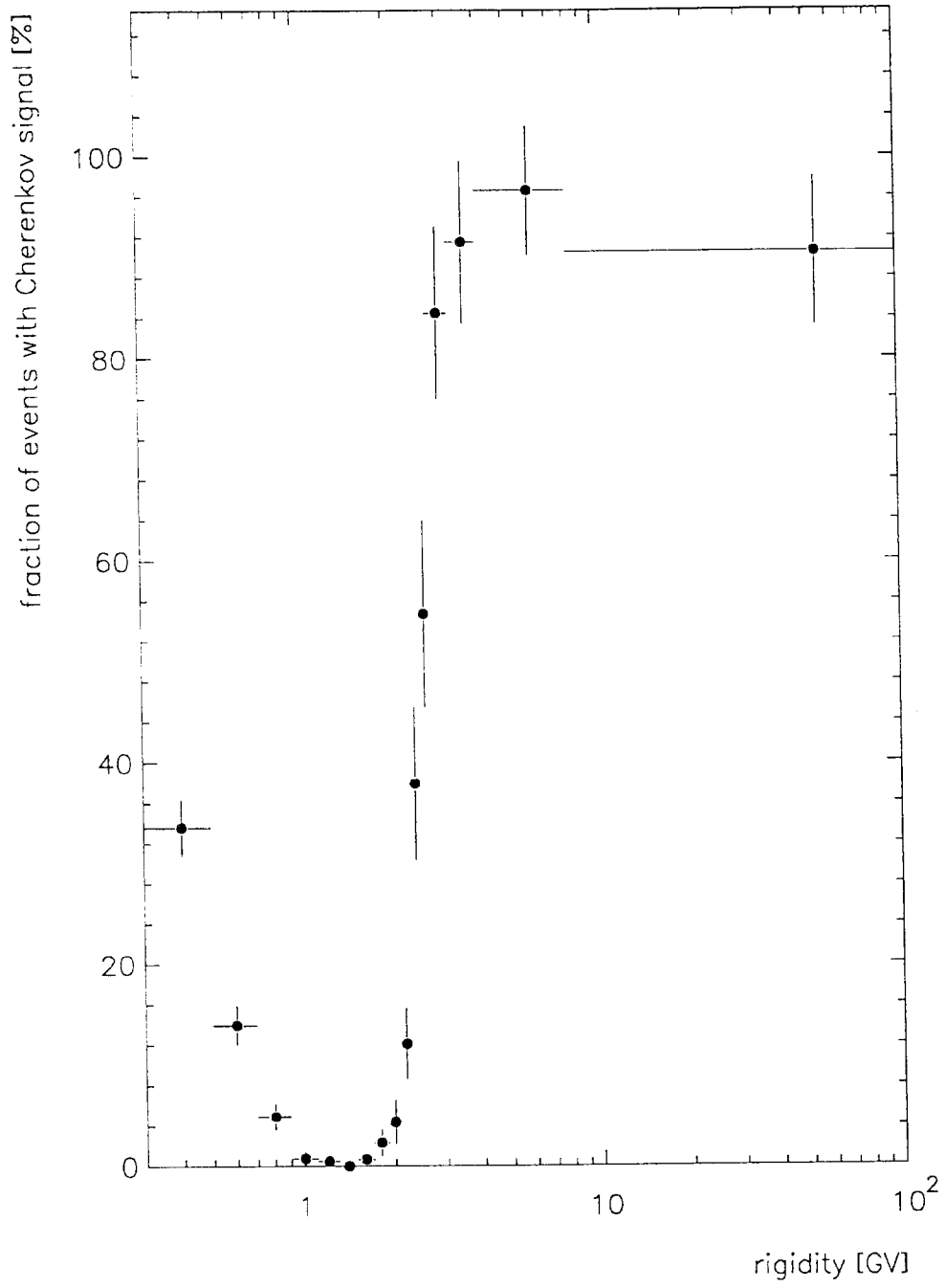


Figure 2

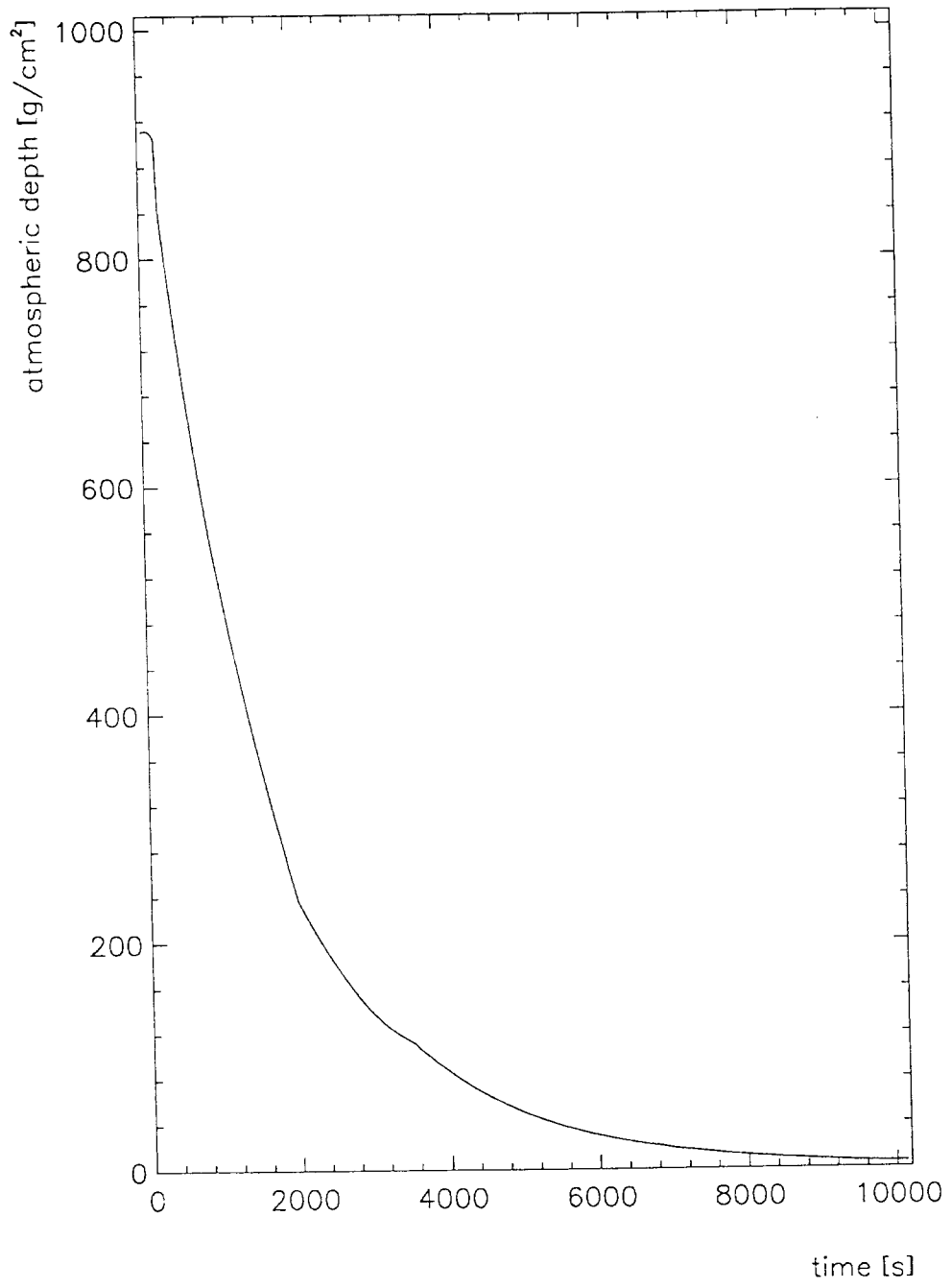


Figure 3

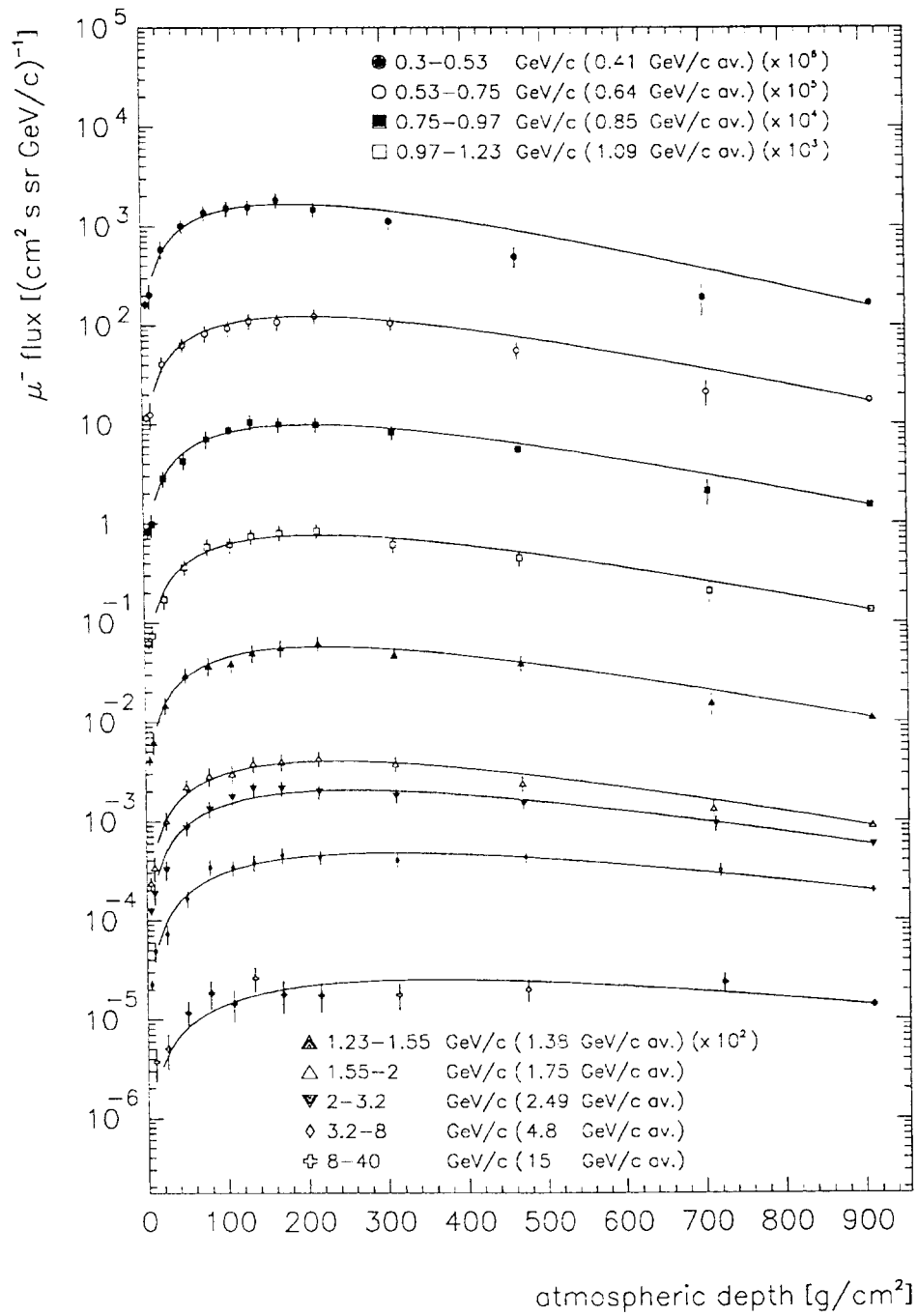


Figure 4

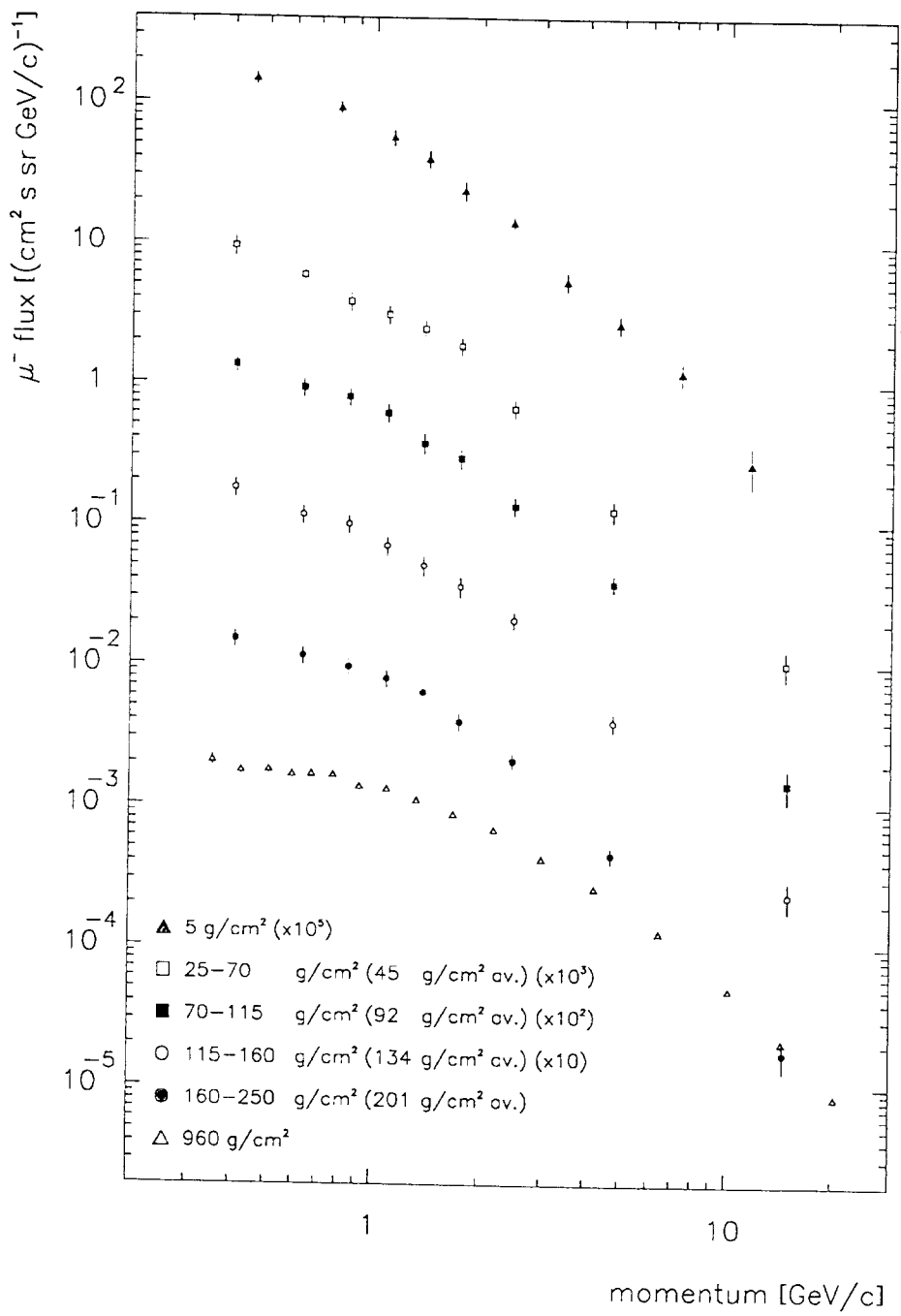


Figure 5